Boron-doped p-BaSi$_2$/n-Si solar cells formed on textured n-Si(001) with a pyramid structure consisting of {111} facets

Tianguo Deng[a], Kazuhiro Gotoh[b], Ryota Takabe[a], Zhihao Xu[a], Suguru Yachi[a], Yudai Yamashita[a],

Kaoru Toko[a], Noritaka Usami[b], Takashi Suemasu[a*]

[a] *Institute of Applied Physics, University of Tsukuba, Tsukuba, Ibaraki 305-8573, Japan*

[b] *Graduate School of Engineering, Nagoya University, Furo-cho, Chikusa-ku, Nagoya 464-8603, Japan*

* Corresponding author.

Electronic mail: suemasu@bk.tsukuba.ac.jp

BaSi$_2$ films were fabricated on textured Si(001) substrates that consisted of {111} facets using molecular beam epitaxy. The light-trapping effect of these films and their performance when incorporated into solar cells were measured. X-ray diffraction and reflectivity measurements showed that the BaSi$_2$ films were grown epitaxially on the textured Si(001) substrate and confirmed the light-trapping effect. The critical thickness over which BaSi$_2$ relaxes increased from approximately 50 to 100 nm when comparing the BaSi$_2$ films on a flat Si(111) substrate and the textured substrate, respectively. p-BaSi$_2$/n-Si solar cells were fabricated with varying BaSi$_2$ layer thickness and with hole concentrations in the range between 2.0×10^{18} and 4.6×10^{18} cm^{-3}. These cells exhibited a maximum energy conversion efficiency of 4.62% with an open-circuit voltage of 0.30 V and a short-circuit current density of 27.6 mA/cm^2 when the p-BaSi$_2$ layer was 75 nm-thick. These results indicated that the use of BaSi$_2$ films on textured Si(001) substrates in solar cells shows great promise.

1. Introduction

A significant amount of work on a wide variety of solar cell materials, including cadmium telluride, chalcopyrite, kesterite, and perovskite, has been performed to realize high energy conversion efficiencies (η) in low-cost solar cells [1-4]. However, many of these materials contain rare and/or toxic elements. Thus, finding suitable absorber materials that are environment-friendly is of great importance. Semiconducting barium disilicide ($BaSi_2$) shows great promise as it has a suitable band gap (1.3 eV) [5-8], a large absorption coefficient (α) of 3×10^4 cm^{-1} at 1.5 eV [6, 9], which is comparable to chalcopyrite, and a large minority-carrier lifetime (τ) of approximately 10 μs [10, 11]. This leads to a large minority-carrier diffusion length (L) of approximately 10 μm, which is much larger than the grain size of $BaSi_2$[12]. An η over 25% is expected for a 2 μm-thick $BaSi_2$ pn junction solar cell [13]. We have previously grown boron (B)-doped p-$BaSi_2$ on a flat n-Si(111) substrate to form pn junction solar cells and achieved an η of 9.9% [14, 15]. Si(111) substrates were used with $BaSi_2$ rather than Si(001) substrates because the oriented a-axis led to a significantly smaller lattice mismatch (approximately 1%) [16], they have inactive grain boundaries [17, 18], and they have a much longer L [19]. However, Si(001) substrates are far more abundant than Si(111) substrates. To attain these favorable features on Si(001) substrates, they can be textured with Si{111} facets by etching. These textured structures have been used to trap incident light, which improves solar cell performance [20-22], with reports of their use in thin-film silicon solar cells with a

high short-circuit current density of 32.9 mA/cm^2 in a single-junction μc-Si:H cell [23].

We have investigated the solar cell performance of p-BaSi$_2$/n-Si heterojunction solar cells. To ensure epitaxial growth of the BaSi$_2$ film on a textured Si(001) substrate and examine the light-trapping effects and solar cell operation, we first grew undoped-BaSi$_2$ films on the textured Si(001) substrate using molecular beam epitaxy (MBE).The morphologies and light trapping behavior of these samples were examined. We then fabricated B-doped p-BaSi$_2$ films on textured n-Si(001) substrates to form p-BaSi$_2$/n-Si solar cells with a p-BaSi$_2$ layer thicknesses (d) from 20 to 125 nm and with hole concentrations (p) from 2.0×10^{18} to 4.6×10^{18} cm^{-3}. The performances of these cells were then examined. A maximum η of 4.62% was achieved when the p-BaSi$_2$ layer thickness was 75 nm and the p was 3.6×10^{18} cm^{-3}.

2. Experimental

An ion-pumped MBE (R-DEC) system with a base pressure less than 10^{-8} Pa was used in this study. This was equipped with an electron-beam evaporation source for Si and standard Knudsen cells for Ba and B. The samples were prepared as follows: first, the (001) surface of a Czochralski n-Si(001) substrate ($\rho = 1-5$ Ωcm) was cleaned by acetone and methanol to eliminate organics followed by dipping in HF/HNO$_3$ mixed acid. Then, the substrate was immersed into SUN-X 600 (Wako) at 75 ºC for 30 min to form a pyramid structure consisting of {111} facets [24], and cleaned by sulfuric acid at 120 ºC for 15 min.   After thermal cleaning

of the substrate, Ba was deposited at 500 °C to form a 5 nm-thick BaSi$_2$ epitaxial template by reactive deposition epitaxy. This template acted as a seed crystal for the growth of the subsequent layer. Ba and Si were co-deposited on the template at 580 °C using MBE to form a BaSi$_2$ epitaxial film that was approximately 400 nm-thick (sample A). The deposition rates of Si and Ba were controlled using an electron impact emission spectroscopy (EIES; INFICON) feedback system. For comparison, another 400 nm-thick BaSi$_2$ epitaxial film was prepared on a flat Si(111) substrate (sample B). The reflectance spectra of samples A and B were compared.

B-doped p-BaSi$_2$/n-Si solar cells with d values ranging from 20 to 125 nm were grown with different sets of B K-cell temperature (T_B) and substrate temperature (T_S). Temperature sets (T_B, T_S) of (1230 °C, 600 °C), (1230 °C, 650 °C), and (1300 °C, 650 °C) were used for samples C, D, and E, respectively. Subsequently, a 3 nm-thick amorphous Si capping layer was prepared at T_S = 180 °C over the BaSi$_2$ layers for all the samples to prevent oxidation of the BaSi$_2$ layer. Pole-figure X-ray diffraction (XRD; RIGAKU, Smart Lab) measurements were performed (Cu Kα radiation) on sample A at $2\theta = 62.42°$ to determine whether the a-axis was normal to the {111} facets. The diffraction angle $2\theta = 62.42°$ allowed for the detection of X-ray diffraction caused by the BaSi$_2$(600) plane. We derived the a-axis lattice constant (a) of the BaSi$_2$ in sample C using the Nelson-Riely relationship [25] with the angle of the sample surface χ fixed at 54.7° with respect to the horizontal plane. The angle $\chi = 54.7°$ corresponds to the angle between the Si(001) and (111) faces. Optical characterizations required sputtering 80 nm-

thick indium-tin-oxide (ITO) electrodes (diameter = 1 mm) on the front surface and 150 nm-thick Al on the back surface. The current density versus voltage (J-V) characteristics under standard AM1.5 illumination and the photoresponse spectra were measured using a xenon lamp with a 25-cm focal-length single monochromator (Bunko Keiki, SM-1700A and RU-60N). The reflectance spectra were evaluated using an integrating sphere. Light intensity was calibrated using a pyroelectric sensor (Melles Griot 13PEM001/J). The morphology of the undoped-$BaSi_2$ surface was observed using field-emission scanning electron microscopy (FE-SEM; HITACHI). Cross-sectional transmission electron microscopy (TEM; FEI, Tecnai Osiris) with an acceleration voltage of 200 kV was used to examine cross sections of the $BaSi_2$ layers on the textured substrate. Thin foils for TEM observation were prepared with an ion beam micro-sampling system. The carrier concentrations of samples C–E were analyzed at ambient temperature via Hall measurements using the van der Pauw method.

3. Results and discussion

SEM images of sample A before and after the growth of the $BaSi_2$ films are shown in Figure 1. Four {111} facets were observed in each pyramid (Fig. 1(b)), with each pyramid being approximately 7 μm. The faces of the $BaSi_2$ were very smooth even after growing a 400 nm-thick $BaSi_2$ film (Fig. 1(c)). However, the four ridgelines of each pyramid and the boundaries between the pyramids were rough, which may have been caused by the coalescence of $BaSi_2$

grains grown on adjacent Si{111} facets. The pole-figure XRD pattern of sample A using BaSi$_2$(600) diffraction ($2\theta = 62.42°$) is shown in Figure 2(a). Four diffraction peaks appeared at $\chi = 54.7°$ as indicated by the four dotted circles. This was confirmed by the φ-scan XRD pattern at $\chi = 54.7°$, shown in Figure. 2(b). Here, φ is the angle of rotation around the normal. These results showed that the a-axis of the BaSi$_2$ was oriented normal to the textured {111} surfaces of the Si (001) substrate.

The reflection spectra of samples A and B are shown in Figure. 3. The reflectance of sample A (BaSi$_2$ film on textured Si(001) substrate) was significantly lower than that of sample B (BaSi$_2$ film on flat Si(111) substrate) over a wide wavelength range, which indicated that light trapping was occurring. On the basis of these promising results, we fabricated and characterized a series of p-BaSi$_2$/n-Si heterojunction solar cells.

We investigated the strain induced in the p-BaSi$_2$ layer when d was varied in films prepared using the conditions used for sample C. The θ-2θ scan XRD spectra obtained at $\chi = 54.7°$ are shown in Figure 4. Diffraction peaks caused by BaSi$_2$ when d was 20 nm were very weak. However, diffraction peaks of (100)-oriented BaSi$_2$ planes, including (200), (400) and (600) planes, were observed when d was 50 nm and above, which indicated the growth of highly a-axis-oriented BaSi$_2$ epitaxial films. Using these three peaks in each sample, the a-axis lattice constants were calculated. The strain ($\Delta a/a$) as a function of BaSi$_2$ film thickness normalized using the sample with the largest d is shown in Figure 5. For comparison, the values of $\Delta a/a$ for

BaSi$_2$ films on the flat substrate were plotted. As the value of d increased from 50 to 100 nm, a

decreased by approximately 0.3%, followed by a slight decrease up to $d = 400$ nm. This

indicated that BaSi$_2$ was under compressive strain along the a axis when $d < 100$ nm, and the

critical thickness over which BaSi$_2$ became relaxed was approximately 100 nm. Interestingly,

the critical thickness increased from approximately 50 nm for a BaSi$_2$ film on the flat Si(111)

substrate to approximately 100 nm for a BaSi$_2$ film on the textured substrate. It is plausible that

the elastic strain energy within the BaSi$_2$ film on the textured substrate was smaller than that

within the film on the flat substrate because the domain size of the BaSi$_2$ was limited to the area

of each {111} facet. Further studies are required to gain a greater understanding of this

phenomenon.

The surface morphology of a 50 nm-thick B-doped p-BaSi$_2$ film on the textured Si(001)

substrate, sample C, was observed using SEM at different magnifications (Fig. 6). The surfaces

of BaSi$_2$, both on the {111} facets and on the ridgelines of the pyramids, were rough (Fig. 6(a)),

while the magnified image (Fig. 6(b)) showed that BaSi$_2$ had layered growth on the facets.

A bright-field (BF) cross-sectional TEM image of sample C with a d value of 50 nm is

shown in Figure 7(a). An electron diffraction (SAED) pattern obtained around the BaSi$_2$/Si

interface area, as indicated by the gray dash circle in Fig. 7(a), is shown in Figure 7(b). The

electron beam was incident along Si[1$\bar{1}$0]. The (100)-oriented diffraction spots of BaSi$_2$,

including (200), (400), and (600), were aligned with the (111)-oriented diffraction spots of Si,

which indicated that the *a*-axis of the p-BaSi$_2$ was grown epitaxially on the {111} facet of the Si. A high-resolution TEM image near the BaSi$_2$/Si interface showed that the BaSi$_2$ film was oriented well and had formed uniformly on the Si substrate with a sharp interface (Fig. 7(c)). However, several steps were observed at the positions marked by the white arrows in Figure 7(d) with a step height in the Si facet of approximately 6 nm. A magnified TEM image around this step is shown in Figure 7(e). Disordered lattices were observed, which may form defective centers for minority carriers. Improved etching techniques will be necessary to avoid these step structures.

J-V curves (AM1.5 illumination) and internal quantum efficiency (*IQE*) spectra for samples C, D, and E with different values of *d* are shown in Figures 8(a)−(f). Their values of *p* were found to be 2.0×10^{18}, 4.6×10^{18}, and 3.6×10^{18} cm^{-3}, respectively. The best properties for each solar cell are summarized in Table.1. p-BaSi$_2$(20 nm)/n-Si solar cells that were fabricated on a flat n-Si(111) substrate[14] with an η of 9.9% are shown for comparison. To accurately obtain the reverse-bias saturation current density (J_0), the shunt resistance (R_{SH}), the series resistance (R_s), and the ideality factor (γ) of the diode, we adopted a technique described in the literature [26]. Using the photodiode equation, these parameters can be given as:

$$\frac{dV}{dJ} = SR_{S} + \frac{\gamma k_{B}T}{q} \left[\frac{1 - (SR_{SH})^{-1} \, dV/dJ}{J + J_{SC} - (SR_{SH})^{-1}V} \right]. \tag{1}$$

where *S* is the device area, k_B is the Boltzmann constant, *T* is the absolute temperature, *q* is the elemental charge, and J_{SC} is the short-circuit current density. We can see from Figures 8(a) and

9

(b) that as d increased from 20 to 125 nm, the solar cell performance initially improved and then degraded with a significant decrease in J_{SC} from 28.4 to 18.8 mA/cm^2. The value of p was 2.0×10^{18} cm^{-3} in sample C. Thus, the J_{SC} reached a maximum at $d = 50$ nm and then decreased. The IQE spectra shown in Figure 8(b) confirmed this.

The contribution of photogenerated carriers in the p-BaSi$_2$ layer became smaller as d increased, especially in the short wavelength range. Similar results were observed for samples D (Fig. 8(d)) and E (Fig. 8(f)), which indicated that as d increased, the photogenerated minority carriers (electrons) within the p-BaSi$_2$ layer were not able to efficiently reach the junction before recombination. Hence, a lower p in the p-BaSi$_2$ layer increased the contribution of p-BaSi$_2$ to the photocurrent. The value of p in sample D was 4.6×10^{18} cm^{-3}. As d increased the η increased to a maximum of 2.66% at $d = 125$ nm (Figs. 8(c) and (d)). The IQE spectrum of the 75 nm-thick sample had the largest IQE over the whole wavelength range. Sample E ($p = 3.6 \times 10^{18}$ cm^{-3}) exhibited a maximum η of 4.62% at $d = 75$ nm (Figs. 8(e) and (f)). Although the reflectance for the BaSi$_2$ film on the textured substrate was smaller (Fig. 3), the highest J_{SC} was limited to 28.5 mA/cm^2 in sample C. This value was significantly lower than that obtained for the p-BaSi$_2$/n-Si solar cells fabricated on the flat Si(111) substrate (35.2 mA/cm^2) [14]. This result suggested that the minority-carrier diffusion length within the p-BaSi$_2$ and/or textured n-Si(001) had degraded. Furthermore, the values of V_{OC} in samples C−E were approximately half of those observed for the devices fabricated on the flat substrate, which indicating that the

BaSi$_2$/Si interfaces was defective. We speculate that BaSi$_2$ grown around the ridge lines of each Si pyramid (Fig. 1(b)) and around the Si steps on the {111} facets (Fig. 7(e)) might be the cause of the lower J_{SC} and V_{OC} parameters. Hence, improvements in η are probable through optimization of the Si surface treatment and growth conditions of the BaSi$_2$ layer.

4. Conclusion

We successfully fabricated BaSi$_2$ films on textured Si (001) substrate with {111} facets. Epitaxial growth of the BaSi$_2$ films was confirmed using XRD and TEM. The critical thickness of the BaSi$_2$ film was approximately 100 nm, which is much larger than for BaSi$_2$ films on a flat Si(111) substrate (50 nm). The reflectance of BaSi$_2$ on the textured substrate was lower than that on the flat substrate, which indicated that light-trapping took place. p-BaSi$_2$/n-Si solar cells with d values between 20 and 125 nm and p values between 2.0×10^{18} and 4.6×10^{18} cm^{-3} were fabricated. A maximum η of 4.62% was observed at $d = 75$ nm.

Figure captions

Fig. 1.   SEM surface images of sample A. (a) Bird's-eye view of the substrate, (b) top-view of the substrate, and (c) 400 nm-thick BaSi$_2$ layer on top of the substrate.

Fig. 2.   (a) Pole-figure XRD pattern of sample A using BaSi$_2$(600) diffraction with $2\theta = 62.42°$. (b) φ-Scan XRD pattern with $\chi = 54.7°$

Fig. 3.   Reflectance spectra of sample A (400 nm-thick undoped-BaSi$_2$ on the textured Si(001) substrate) and of sample B (400 nm-thick undoped BaSi$_2$ on the flat Si(111) substrate).

Fig. 4. θ-2θ XRD spectra of B-doped p-BaSi$_2$ films (sample C) with d values from 20 to 400 nm. The angle χ was set at 54.7°, which corresponds to the angle between the Si(001) and Si(111) planes.

Fig. 5. Normalized strain ($\Delta a/a$) as a function of film thickness (d) for the B-doped p-BaSi$_2$ layers on the textured Si(001) and flat Si(111) substrates.

Fig. 6.   SEM surface images of (a) 50 nm-thick B-doped p-BaSi$_2$ on the textured substrate, sample C, and (b) a magnified image of the area marked by the black dash circle in (a).

Fig.7. (a) BF TEM cross sections of a 50 nm-thick B-doped p-BaSi$_2$ film near the top of the Si pyramid. (b) SAED pattern near the p-BaSi$_2$ /Si interface area indicated by the gray dash circle in (a) (The electron beam was incident along Si[$1\bar{1}0$]. The white dotted line is shown as a guide.) (c) High-resolution TEM image near the p-BaSi$_2$ /Si interface. (d) BF TEM cross section of a step with a height of approximately 6 nm, as indicated by white arrows. (e) High-resolution TEM image of the area marked by a white dash circle in (d).

Fig. 8. *J-V* curves under AM1.5 illumination and *IQE* spectra of sample C ((a) and (b)), sample D ((c) and (d)), and sample E ((e) and (f)).

References

[1] M. Gloeckler, I. Sankin, Z. Zhao, IEEE Journal of Photovoltaics 3 (2013) 1389-1393.

[2] P. Reinhard, A. Chirilă, P. Blösch, F. Pianezzi, S. Nishiwaki, S. Buechelers, A.N. Tiwari, in: 2012 IEEE 38th Photovoltaic Specialists Conference (PVSC) PART 2, 2012, pp. 1-9.

[3] G. Niu, X. Guo, L. Wang, J. Mater. Chem. A 3 (2015) 8970-8980.

[4] M. A. Green, K. Emery, Y. Hishikawa, W. Warta, E.D. Dunlop, Progress in Photovoltaics: Research and Applications 24 (2016) 3-11.

[5] K. Morita, Y. Inomata, T. Suemasu, Thin Solid Films 508 (2006) 363-366.

[6] K. Toh, T. Saito, T. Suemasu, Japanese Journal of Applied Physics 50 (2011) 068001.

[7] M. Kumar, N. Umezawa, M. Imai, Applied Physics Express 7 (2014) 071203.

[8] T. Suemasu, N. Usami, Journal of Physics D: Applied Physics 50 (2017) 023001.

[9] D. B. Migas, V. L. Shaposhnikov, V. E. Borisenko, physica status solidi (b) 244 (2007) 2611-2618.

[10] K. O. Hara, N. Usami, K. Nakamura, R. Takabe, M. Baba, K. Toko, T. Suemasu, Applied Physics Express 6 (2013) 112302.

[11] K.O. Hara, N. Usami, K. Toh, M. Baba, K. Toko, T. Suemasu, Journal of Applied Physics 112 (2012) 083108.

[12] M. Baba, K. Toh, K. Toko, N. Saito, N. Yoshizawa, K. Jiptner, T. Sekiguchi, K.O. Hara, N. Usami, T. Suemasu, Journal of Crystal Growth 348 (2012) 75-79.

[13] T. Suemasu, Japanese Journal of Applied Physics 54 (2015) 07JA01.

[14] S. Yachi, R. Takabe, H. Takeuchi, K. Toko, T. Suemasu, Applied Physics Letters 109 (2016) 072103.

[15] D. Tsukahara, S. Yachi, H. Takeuchi, R. Takabe, W. Du, M. Baba, Y. Li, K. Toko, N. Usami, T. Suemasu, Applied Physics Letters 108 (2016) 152101.

[16] R. A. McKee, F. J. Walker, J. R. Conner, R. Raj, Applied Physics Letters 63 (1993) 2818-2820.

[17] M. Baba, S. Tsurekawa, K. Watanabe, W. Du, K. Toko, K.O. Hara, N. Usami, T. Sekiguchi, T. Suemasu, Applied Physics Letters 103 (2013) 142113.

[18] M. Baba, M. Kohyama, T. Suemasu, Journal of Applied Physics 120 (2016) 085311.

[19] M. Baba, K. Watanabe, K.O. Hara, K. Toko, T. Sekiguchi, N. Usami, T. Suemasu, Japanese Journal of Applied Physics 53 (2014) 078004.

[20] Y. Inomata, T. Nakamura, T. Suemasu, F. Hasegawa, Japanese Journal of Applied Physics 43 (2004) L478-L481.

[21] M. Despeisse, G. Bugnon, A. Feltrin, M. Stueckelberger, P. Cuony, F. Meillaud, A. Billet, C. Ballif, Applied Physics Letters 96 (2010) 073507.

[22] F. J. Haug, K. Söderström, A. Naqavi, C. Ballif, Journal of Applied Physics, 109 (2011) 084516.

[23] H. Sai, T. Matsui, T. Koida, K. Matsubara, M. Kondo, S. Sugiyama, H. Katayama, Y. Takeuchi, I. Yoshida, Applied Physics Letters 106 (2015) 213902.

[24] T. Tayagaki, D. Furuta, O. Aonuma, I. Takahashi, Y. Hoshi, Y. Kurokawa, N. Usami, Japanese Journal of Applied Physics 56 (2017) 04CS01.

[25] J. B. Nelson, D. P. Riley, Proceedings of the Physical Society 57 (1945) 160.
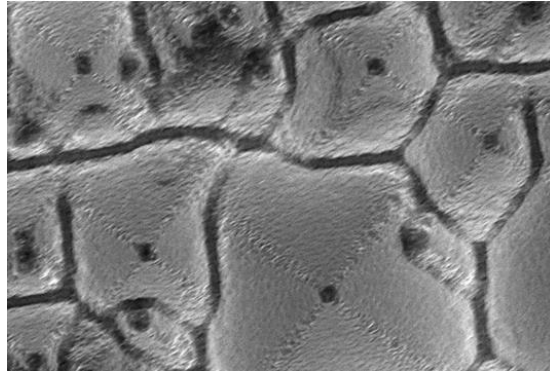
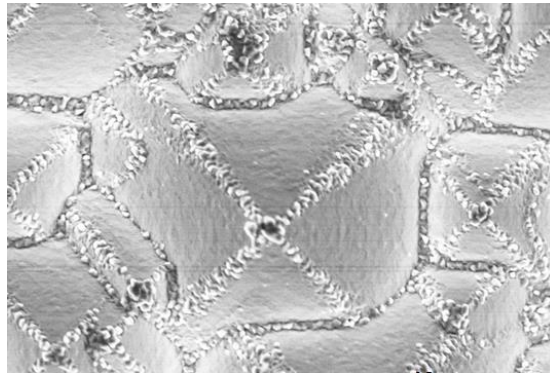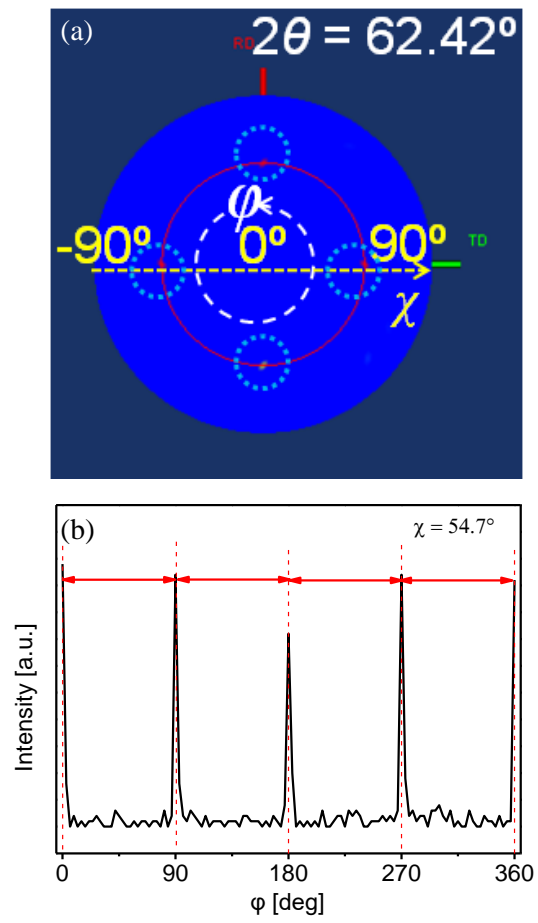[26] J. R. Sites, P. H. Mauk, Solar Cells 27 (1989) 411-417.

(a)

10 μm

(b)

10 μm

(c)
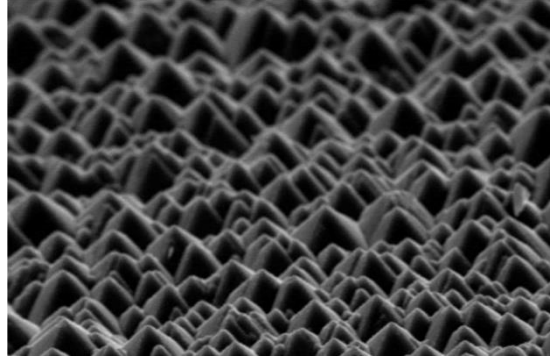
10 μm

Fig. 1

Fig. 2
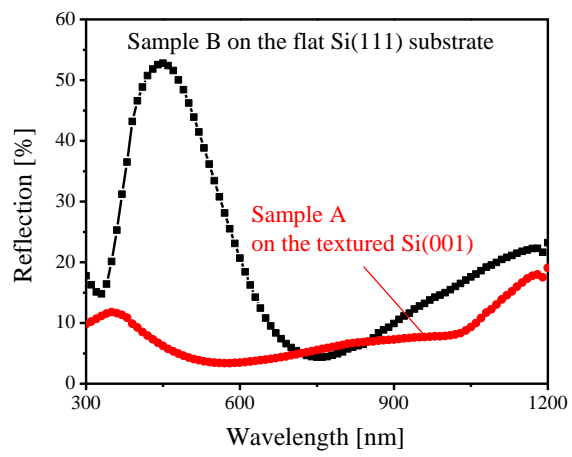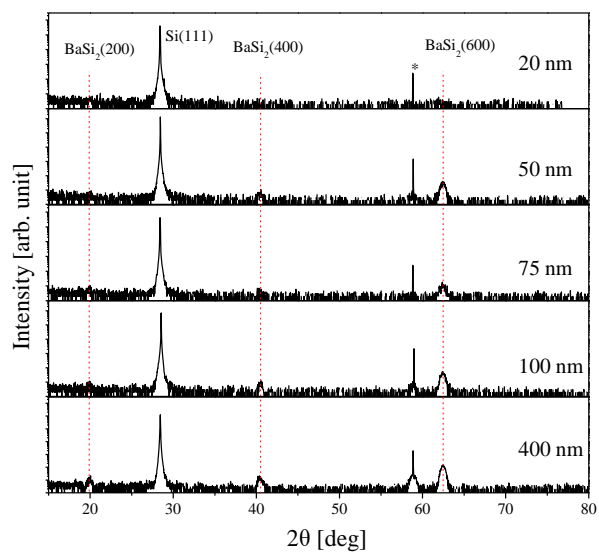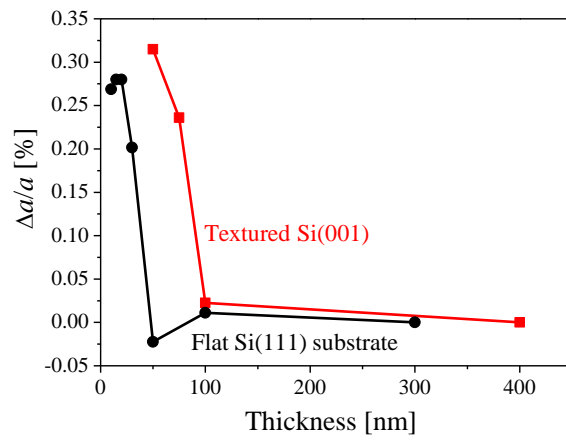
Fig. 3

Fig. 4

Fig. 5

(a)

5 μm

(b)

2 μm

Fig. 6

(a)

BaSi$_2$

Si

0.5 μm

(b)

(100)$_{BaSi_2}$ // (111)$_{Si}$

BaSi$_2$
600→
400→
200→
Si
111

O

(c)

BaSi$_2$

Si

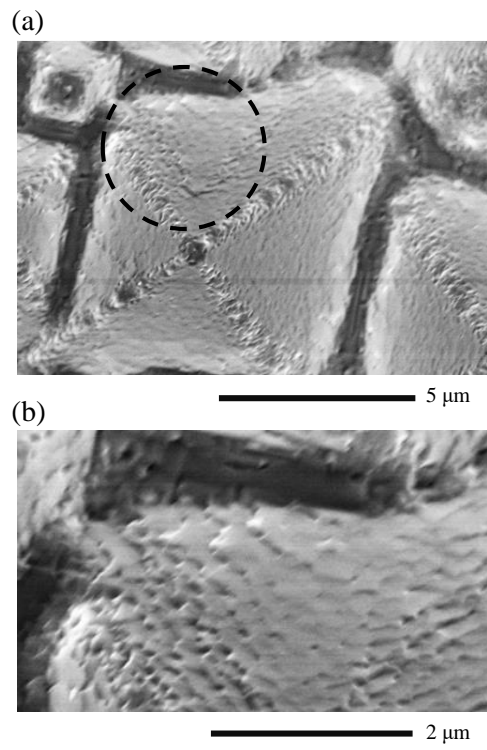10 nm

(d)

BaSi$_2$
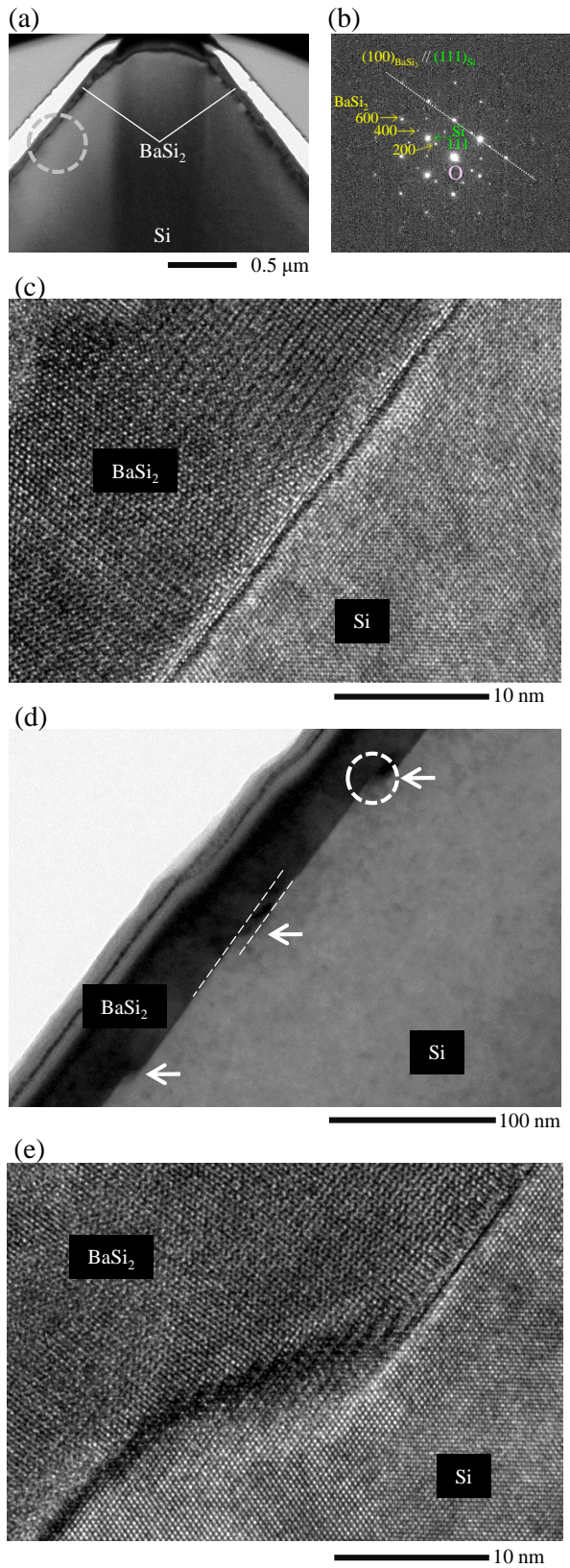
Si

100 nm

(e)
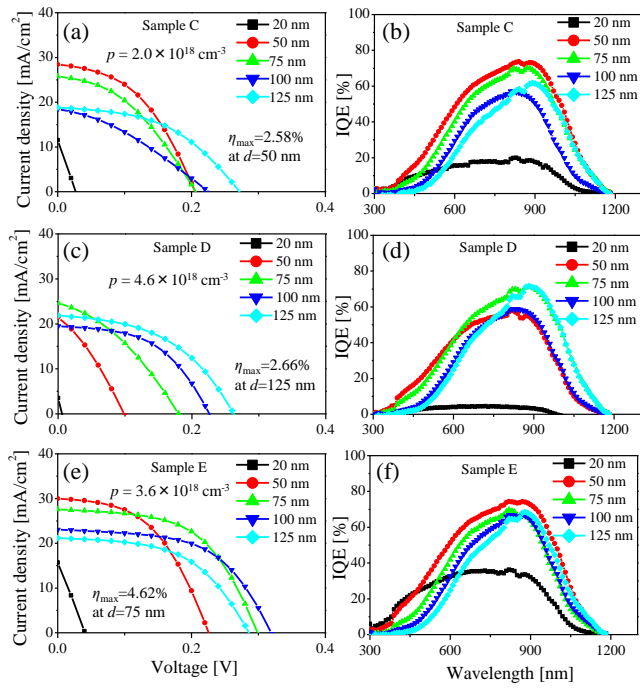
BaSi$_2$

Si

10 nm

Fig. 7

Fig. 8

Table 1 Solar cell properties of the best solar cell in each sample are specified. For comparison, those of p-BaSi$_2$/n-Si solar cells on a flat Si(111) [14] are shown.

Sample	d [nm]	J_{SC} [mA/cm^2]	V_{OC} [V]	FF [%]	η [%]	R_S [Ω]	R_{SH} [Ω]	γ	J_0 [mA/cm^2]
C	50	28.5	0.20	44.3	2.58	209	30476	1.16	2.42×10^{-4}
D	125	21.8	0.26	46.4	2.66	256	43182	2.65	3.15×10^{-3}
E	75	27.6	0.30	54.9	4.62	208	61839	1.23	1.68×10^{-5}
Reference [14]	20	35.2	0.47	60.0	9.9	128	10046	1.17	1.49×10^{-5}